Superradiant emission in a high-mobility two-dimensional electron gas

IOP Publishing Journal of Physics: Condensed Matter
J. Phys.: Condens. Matter **35** (2023) 305302 (9pp) https://doi.org/10.1088/1361-648X/acce8c

Superradiant emission in a high-mobility two-dimensional electron gas

B Barman[1,2], A G Linn[2], A L O'Beirne[2], J Holleman[3], C Garcia[3], V Mapara[4], J L Reno[5], S A McGill[3], V Turkowski[6], D Karaiskaj[4] and D J Hilton[7,*]

[1] College of Innovation and Technology, University of Michigan-Flint, Flint, MI 48502, United States of America
[2] Department of Physics, University of Alabama at Birmingham, Birmingham, AL 35294-1170, United States of America
[3] National High Magnetic Field Laboratory, Florida State University, Tallahassee, FL 30201, United States of America
[4] Department of Physics, University of South Florida, Tampa, FL 33620, United States of America
[5] Center for Integrated Nanotechnologies, Sandia National Laboratory, Albuquerque, NM 87185, United States of America
[6] Department of Physics, University of Central Florida, Orlando, FL 32816, United States of America
[7] Department of Physics, Baylor University, Waco, TX 76798-7316, United States of America

E-mail: David_Hilton@baylor.edu

Received 5 December 2022, revised 31 March 2023
Accepted for publication 19 April 2023
Published 28 April 2023

Abstract

We use terahertz time-domain spectroscopy to study gallium arsenide two-dimensional electron gas samples in external magnetic field. We measure cyclotron decay as a function of temperature from 0.4 to 10 K and a quantum confinement dependence of the cyclotron decay time below $T_0 = 1.2$ K. In the wider quantum well, we observe a dramatic enhancement in the decay time due to the reduction in dephasing and the concomitant enhancement of superradiant decay in these systems. We show that the dephasing time in 2DEG's depends on both the scattering *rate* and also on the distribution of scattering angles.

Keywords: quantum well, cyclotron resonance spectroscopy, many-body effects, two-dimensional electron gas, dicke superradiant emission

(Some figures may appear in colour only in the online journal)

1. Introduction

Collective excitations dominate both the electronic and optical properties in many condensed matter systems and have been studied extensively in both bulk and nanoscale geometries [1–6]. Excitons [2, 7], trions [8], biexcitons [3], and other higher order quasiparticles [5] are expected to be significant in nanoscale systems (e.g. quantum wells, quantum dots) and two-dimensional materials like transition metal dichalcogenides [8, 9], silcene [10], germanene [11], stanene [12], and phosphorus [13, 14]. They have been shown to dominate the electronic properties at room temperature in the monolayer transition metal dichalcogenides, where the reduced electronic screening in a monolayer results in larger quasiparticle binding energies [4, 6].

Superradiant emission is a cooperative emission from an ensemble of noninteracting dipoles [15]. Ensemble coherence is established by an external electromagnetic field with a wavelength that is much larger than the distance between dipoles. The key requirement for the observation of superradiant emission is that this coherence be maintained for longer than the emission lifetime. This phenomena has been observed in many different physical situations at

* Author to whom any correspondence should be addressed.

vastly different scales (i.e. from the nanoscale to astrophysical scale). In condensed matter systems, this includes electron–hole plasmas in semiconductors [16], excitons [17], and bulk semiconductors [18]. Superradiant emission has also been observed in optically-pumped gasses [19] and in radio frequency astrophysics [20, 21]. Nanoscale systems like quantum dots [22] and two-dimensional quantum wells [23, 24] also exhibit superradiant emission, where the degree of quantum confinement is an additional method for controlling this collective emission.

In this manuscript, we study superradiant emission in Landau-quantized two-dimensional electron gas (2DEG) samples to determine the role of quantum confinement on light emission. We use terahertz time-domain magnetospectroscopy to measure the cyclotron decay time, τ_{CR}, in a pair of 2DEG quantum well samples as a function of temperature and quantum well width. Our experimental data shows close agreement in measured values of τ_{CR} in both samples *above* $T_0 = 1.2\,\mathrm{K}$. Below this temperature, however, the wide quantum well shows a $\sim 3.0\times$ *increase* in the decay time while the narrow quantum well *decreases* by $1.5\times$. A theoretical description of our data shows that our result is consistent with the enhancement of the density of states near $\mathcal{E}_F$ in the strongly confined well. In addition, in the wider quantum well, the narrowing of the angular dependence of scattering distribution dominates dephasing and is responsible for an increase in the dephasing time at the lowest temperatures in our experiments.

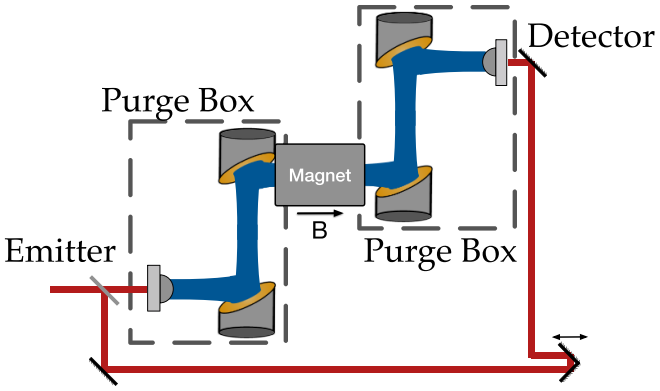

Figure 1. The terahertz time-domain spectrometer geometry used in these experiments is shown here. An 80. MHz repetition rate mode-locked titanium:sapphire laser photoexcites a photoconductive emitter [28], which generates a linearly polarized ($\hat{x}$) near-single cycle terahertz pulse with a bandwidth from 0.2 to 1.9 THz. The terahertz pulse, $E(\tau)$, is transmitted through the superconducting magnet using a pair of off-axis parabolic mirrors (OAP) in Faraday geometry ($\vec{B} \parallel \vec{k}$). The copolarized ($\hat{x}$) component of the transmitted field is detected by a time-gated photoconductive receiver to resolve the transmitted electric field.

2. Experiments

2.1. Terahertz time-domain spectroscopy (TTDS)

We use TTDS to measure cyclotron resonance in these two samples [25, 26]. These samples were placed in a 10 T superconducting optical magnet cryostat (Oxford Instruments SpectroMag with a ^{3}He insert) having a base temperature of 0.4 K in the Faraday geometry (i.e. $\vec{k} \parallel \vec{B}$). Coherent single cycle THz pulses were generated and detected by focusing the 800 nm beam of a Ti:Sapphire oscillator, operating at 80 MHz and with approximately 0.120 ps pulse duration onto a pair of biased photoconductive antennae. The resulting THz radiation has a bandwidth range from 0.2 to 1.9 THz. We used off-axis parabolic mirrors to direct the THz beam and collect the transmitted light through the Spectrosil B windows of the magnet. An LT-GaAs photoconductive receiver is used as our detector to recover the full amplitude and phase of the transmitted terahertz electric field as a function of $\vec{B}$ and temperature in all samples [27].

Figure 1(b) shows a diagram of our terahertz time-domain spectrometer, which generates and detects linearly-polarized sub-picosecond terahertz pulses, $\vec{E}_i(\tau) = \hat{x}E_0(\tau)$, with a photoconductive emitter and detector [28]. We use an Oxford Instruments SpectroMag split-coil magnet that has a base temperature of $T = 0.4\,\mathrm{K}$ to generate an external magnetic field, $\vec{B}$. These experiments are performed in the Faraday geometry ($\vec{B} \parallel \vec{k}$), where $\vec{B} = \mathbf{B}_0\hat{z}$ is the magnetic field, $\vec{k} = +\kappa_0\hat{z}$ is the THz pulse propagation vector, and the 2DEG samples are defined to be in the $\hat{x}$-$\hat{y}$ plane. Our apparatus has a bandwidth that extends from 0.2 THz to 1.9 THz and is operated in a dry nitrogen atmosphere to minimize the effects of water vapor absorption on our experimental data [29].

2.2. Samples studied

The two samples studied here are modulation doped GaAs single quantum wells with AlGaAs barriers. Both samples are grown via Molecular Beam Epitaxy [30]: Sample VA0607 ($\mu_{DC} = 1.5\times10^5\,\mathrm{cm^2\,V^{-1}\,s^{-1}}$ and $n_s = 1.7\pm0.1\times10^{11}\,\mathrm{cm^{-2}}$) has a well width of 12 nm and that of Sample EA0745 ($\mu_{DC} = 3.6\times10^6\,\mathrm{cm^2\,V^{-1}\,s^{-1}}$ and $n_s = 1.5\pm0.1\times10^{11}\,\mathrm{cm^{-2}}$) is 30 nm [24]. The carrier concentration in both samples result from δ-doping separated from the quantum well by $Al_{0.24}$ Ga $_{0.76}$ As barrier layers with thicknesses of $d_1 = 75$ nm and $d_2 = 95$ nm in both samples. This δ-doping is a geometry that is known to prevent a sharp decrease in the carrier concentration at low temperatures (i.e. 'freeze out') [31], so these are expected to remain conducting throughout the entire temperature range of our experiments ($0.4\,\mathrm{K} \leqslant T \leqslant 10\,\mathrm{K}$).

Doped quantum wells as a prototype 2DEG model system have been previously studied using many techniques, including cyclotron resonance. Figure 2 plots the carrier concentration (n_s) and mobility (μ_{DC}) of GaAs quantum well samples that have been previously studied using cyclotron resonance [23–26, 32–42] Prior investigation of sample EA0745 was described in [23], with the difference for our manuscript being the comparison between this sample and a narrower QW (VA0607). Molecular beam epitaxy produces GaAs 2DEG's with mobilities that range from $\mu_{DC} = 4\times10^3\,\mathrm{cm^2\,V^{-1}\,s^{-1}}$ [30, 37] to $\mu_{DC} = 4.4\times10^7\,\mathrm{cm^2\,V^{-1}\,s^{-1}}$ [43] and has demonstrated mobilities that approach the intrinsic limits of gallium arsenide [44]. The samples previously studied are plotted

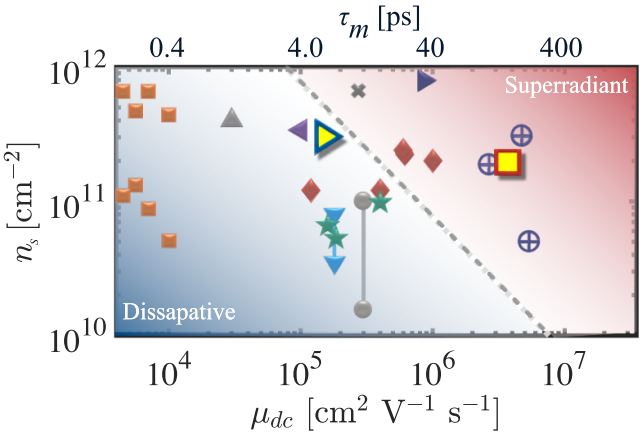

Figure 2. (b) The cyclotron resonance has been previously performed on GaAs 2DEG's, which are identified using the carrier concentration, n_s, and the mobility, μ_{DC}. The dotted line plots the curve where $\tau_m = \tau_{SR}$ in these samples and represents an approximate dividing in between the two pathways.

using their values of n_s and μ_{DC} using × [32], ◀ [33], ▲ [34], ♦ [35], ★ [36], ■ [37], ▶ [38], ⊕ [23], and □ [23–26].

Figure 2 plots the line where the superradiant decay time, τ_{SR}, is equal to the transport lifetime, $\tau_m = \mu_{DC} m^* e^{-1}$ (dotted line) as an approximate boundary to divide the parameter space between the two contributions to τ_{CR} [23]. Below this line, dissipation returns the sample to its ground state; this includes a majority of prior experiments [33–37, 39, 40]. Above, superradiant emission is the main contribution [24, 25], but many prior studies did not recognize this collective contribution in their data (× [32], ♦ [35], ▶ [38]). The high mobility-high carrier concentration region, thus, represents a significant current gap in our understanding of 2D cyclotron resonance.

2.3. Experimental data and numerical fitting

Figures 3(a) and (b) shows the change to the transmitted THz waveform through VA0607 (a) and EA0745 (b) in a magnetic field of $B_z = 0.8\,\mathrm{T}$ at $T = 0.4\,\mathrm{K}$. We isolate the magnetic field-induced change, $\Delta E(B_z,\tau) = E(B_z,\tau) - E(0,\tau)$, by subtracting the waveform acquired at 0 T [25]. We repeat this experiment from $T = 0.4\,\mathrm{K}$ to 10 K to determine the temperature dependence of the cyclotron frequency, ν_{CR}, the cyclotron decay time, τ_{CR}, and the arrival time, τ_0. The satellite pulse at approximately $\tau = 15\,\mathrm{ps}$ after the initial terahertz pulse is generated by the substrate multiple reflection (Fabry–Perot etalon).

We use the procedure outlined in [45] to determine the cyclotron decay time from our experimental data shown in figure 3. Figure 4(a) plots the cyclotron decay times as a function of temperature in both samples and shows similar decay dynamics for $T_0 \geq 1.2\,\mathrm{K}$ at $|\vec{B}| = 0.8\,\mathrm{T}$. Below this temperature, τ_{CR} in VA0607 monotonically decreases as the temperature is lowered by a factor of 1.5 × at 0.4 K. In EA0745, in contrast, over the same temperature range τ_{CR} increases by 3.0 ×. The increase in quantum confinement reduces the cyclotron decay time at low temperatures. The focus of our discussion

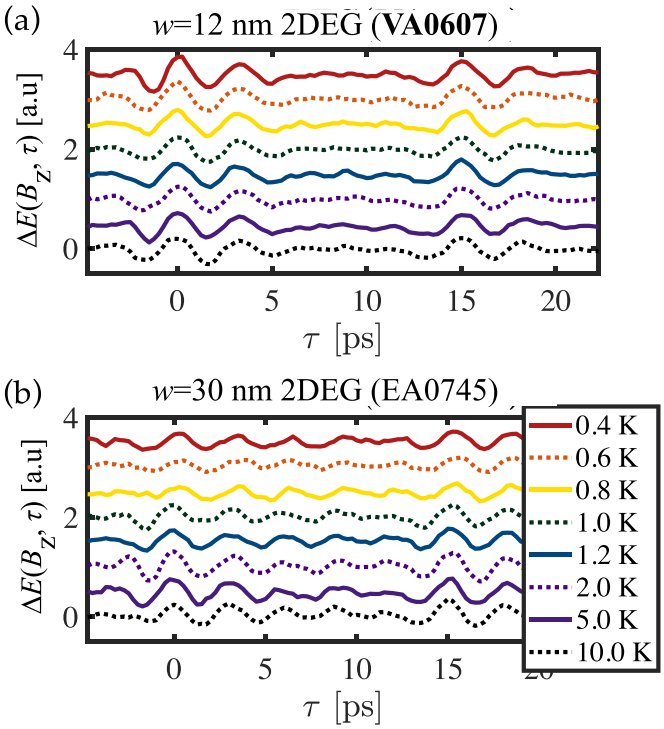

Figure 3. (a) VA0607 data (b) EA0745 data at $B_z = +0.8\,\mathrm{T}$ are plotted here at $T = 0.4\,\mathrm{K}$. A time-delayed echo is present at $\tau \approx 15\,\mathrm{ps}$ due to a Fabry–Perot etalon in the GaAs substrate, which we account for in our modeling of these data [45].

will be to elucidate the observed temperature-dependence in τ_{CR} in these two different samples.

2.4. Isolation of dephasing and superradiant emission lifetimes

The cyclotron decay rate (τ_{CR}^{-1}) is the oscillation decay time in our terahertz time-domain experiments. This is a combination of the superradiant emission rate (τ_{SR}^{-1}) and the dephasing rate ($\tau_2{}^{-1}$)[8] and is schematically depicted in figure 4(b). Superradiant decay is the transfer of energy from the Landau spectrum back into the terahertz field, which preserves system coherence, and can be only observed when the dephasing rate (thermodynamic bath) is slower. Experimental investigation of superradiant decay, thus, requires the use of a sample with dephasing times of several picoseconds (ps) or longer (i.e. $\mu_{DC} \geq 10^4\,\mathrm{cm^2\,V^{-1}\,s^{-1}}$) for typical carrier concentrations in 2DEG's (i.e. $n_s = 10^{10}$ to $10^{12}\,\mathrm{cm^{-2}}$). This restriction currently limits investigations of superradiant decay to the traditional semiconductor 2D systems (e.g. GaAs and Si) due to the limited availability of large samples of high mobility transition metal dichalcogenides[9].

Superradiant emission preserves system (i.e. light and matter) coherence. We isolate this contribution to τ_{CR} first and the

[8] With our experimental configuration, it is not possible to distinguish τ_2 (homogeneous) and τ_2^* (inhomogeneous).

[9] See, for example, [9], which recently demonstrated field effect transistors from wafer scale MoS_2 with a mobility of only $\mu_{DC} = 82\,\mathrm{cm^2\,V^{-1}\,s^{-1}}$.

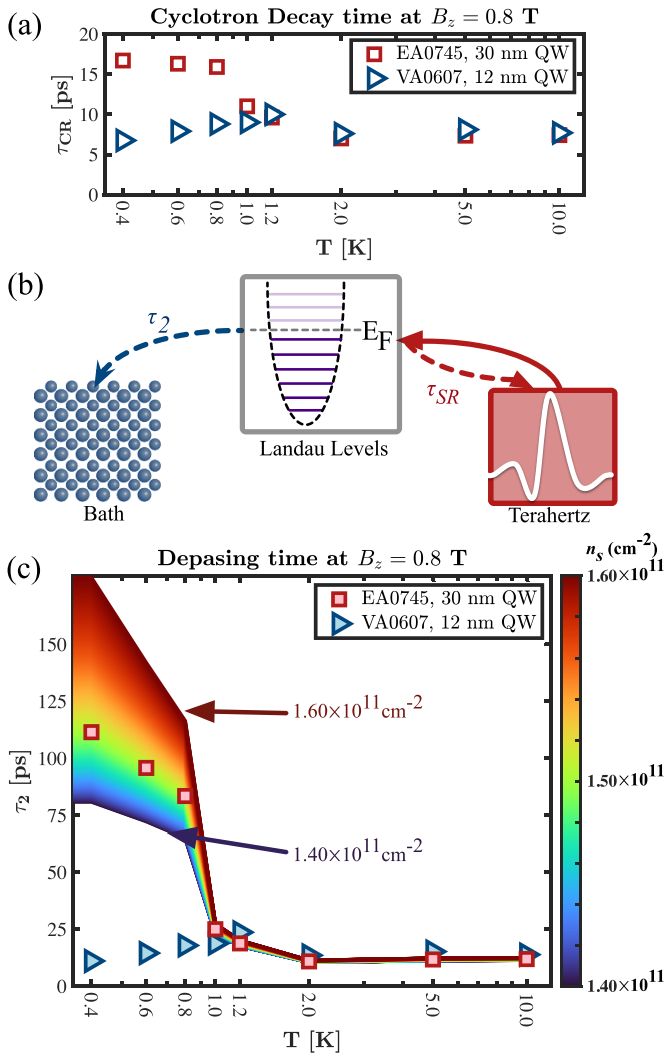

Figure 4. (a) Superradiant emission couples the Landau spectrum back into the terahertz field (τ_{SR}) while dissipation (τ_2) couples to a thermodynamic bath. (b) The cyclotron decay time, τ_{CR}, for each sample obtained using the fitting procedure described in [45]. (c) Calculating τ_{SR}, we determine the temperature-dependent dephasing time, τ_2, in both samples. The range of values is related to the uncertainty in n_s, which is discussed in the text and included only for EA0745 in this plot as the fan of curves around EA0745 (□). Because the values for VA0607 are due to dissipative processes alone, the uncertainty in n_s does not significantly contribute to the value of τ_2.

residual contribution will be $\tau_2(T)$. This superradiant emission time, τ_{SR}, is given by equation (1).

$$\frac{1}{\tau_{SR}} = \frac{e^2}{\epsilon_0 c}\frac{n_s}{m^*(n_{GaAs}+1)}. \tag{1}$$

This depends on the electron charge (e), the speed of light in vacuum (c), and the free space permittivity (ϵ_0), as well as materials-specific properties: the terahertz-frequency refractive index (n_{GaAs}), effective mass (m^*), and the cyclotron sheet carrier concentration (n_s). Each material parameter has been previously shown to vary in GaAs 2DEG's under different experimental conditions (e.g. quantum confinement, B_z, and T) [34, 35, 39]. First, we use $\nu_{CR} = \frac{eB_z}{m^*}$ in sample VA0607 to find $m^* = 0.0696 \pm 0.0014$. Sample EA0745 was previously characterized using this experimental technique and also did not show a temperature-dependent m^* [26]. Second, we use the *pulse arrival time*, τ_0, to determine the temperature-dependent refractive index, n_{GaAs}. This pulse is detected using a time-gated electro-optic detection after transmission through the 2DEG sample, so a change in arrival time would be the result of a change in n_{GaAs}. We observe no variation in τ_0 as a function of temperature in either sample for all temperatures measured; any changes to n_{GaAs} are below our system resolution; if we assume a minimum resolvable time step of 50 fs in these data, the relative change in refractive index is $\Delta n_{GaAs}/n_{GaAs} \leqslant 0.07\%$. Finally, modulation-doped 2DEG's rely on spatially separated δ-doped silicon layers near the undoped well. This results in a fixed carrier concentration, n_s, that is spatially separated from the dopant and that does not freeze out at low temperatures [31].

Uncertainty in n_s limits the *accuracy* of τ_{SR} via (1). This is the largest source of uncertainty in our determination of $\tau_2(T)$. If we assume that $\Delta n_s = 0.1 \times 10^{11}\,\mathrm{cm}^{-2}$ at 0.4 K, we can estimate the resulting uncertainty in τ_{SR} to determine if the observed temperature-dependence is significant. We find τ_{SR} in VA0607 is 12.3 ± 1.4 ps while τ_{SR} is 17.3 ± 1.0 ps in EA0745. The $\tau_2(T)$ determined from this and our τ_{CR} data is shown in figure 4(b) for both samples [46]. In EA0745 where τ_{SR} is dominant, we plot τ_2 for a range of n_s within our uncertainty, where the curves of constant color correspond to specified values of n_s. We find $80.9\,\mathrm{ps} \leqslant \tau_2(T) \leqslant 179.3\,\mathrm{ps}$ in EA0745 and $10.7\,\mathrm{ps} \leqslant \tau_2(T) \leqslant 11.5\,\mathrm{ps}$ in VA0607 at $T = 0.4$ K. As the carrier concentration is a single parameter in all of the τ_{SR} calculations, the uncertainty in n_s results in a systematic shift in the entire $\tau_2(T)$ curve within the uncertainty range. We find that the *trend* toward longer dephasing times in EA0745 when compared to the VA0607 below T_0 is clearly preserved.

3. Theoretical methods

The dephasing time, τ_2, depending on two main contributions. First, the scattering rate, Γ, that results in the change in momentum of the electron, which is discussed in section 3.1. The second key contribution is the phase error accumulated with each scattering event, which depends on the distribution of scattering angles, $S(\vartheta)$ and is discussed in section 3.2.

3.1. Derivation of electron–electron scattering time

We determine the electron–electron scattering time, τ_{ee}, starting with the appropriate Boltzmann equation:

$$e\vec{E}\frac{\partial f}{\partial \vec{k}_1} = \left(\frac{\partial f}{\partial t}\right)_{e-e} + \left(\frac{\partial f}{\partial t}\right)_{p,i} \tag{2}$$

where the first term on the right hand side is the electron–electron scattering contribution and the second term are those

contributions that result from phonon and impurity scattering. In our calculation, we focus on the dimensionality-dependence of the electron–electron scattering rate. The solution to (2) is given by (3)

$$f(\vec{\mathrm{k}}_1) = f_0(\vec{\mathrm{k}}_1) + f_0(\vec{\mathrm{k}}_1)\left[1 - f_0(\vec{\mathrm{k}}_1)\right]\Psi(\vec{\mathrm{k}}_1). \tag{3}$$

Here, f_0 is the non-interacting distribution function given by:

$$f_0\left(\vec{\mathrm{k}}_1\right) = \left[\exp\left(\frac{\mathcal{E}(\vec{\mathrm{k}}_1) - \mathcal{E}_\mathrm{F}}{k_\mathrm{B}T}\right) + 1\right]^{-1} \tag{4}$$

where $\mathcal{E}(\vec{\mathrm{k}}_1)$ is the energy at $\vec{\mathrm{k}}_1$, k_B is the Boltzmann constant, T is the system temperature, and $\mathcal{E}_\mathrm{F} = \frac{\hbar^2 k_\mathrm{F}}{2m^*}$ is the Fermi Energy. $\Psi(\vec{\mathrm{k}}_1)$ is determined by the angle, $\vartheta_{\vec{\mathrm{k}}_1}$ between the electric field, $\vec{E}$, and the electron quasimomentum, $\vec{\mathrm{k}}_1$

$$\Psi\left(\vec{\mathrm{k}}_1\right) = \sum_{n=1}^{\infty} \psi_n(\vec{\mathrm{k}}_1)\cos\left(\vartheta_{\vec{\mathrm{k}}_1}\right). \tag{5}$$

From this term, we determine the linearized electron–electron scattering operator, $\hat{I}_{ee}[\Psi]$, which is given by:

$$\begin{aligned}\hat{I}_{ee}\left[\psi_1\cos\left(\vartheta_{\vec{\mathrm{k}}_1}\right)\right] = -2\int \frac{d^n k_2}{(2\pi)^n}\int \frac{d^n q}{(2\pi)^n}\bar{w} \\ \times \left(\vec{\mathrm{k}}_1 + \vec{\mathrm{q}}, \vec{\mathrm{k}}_2 - \vec{\mathrm{q}}; \vec{\mathrm{k}}_1, \vec{\mathrm{k}}_2\right) f_0(\vec{\mathrm{k}}_1) f_0(\vec{\mathrm{k}}_2) \\ \times \left[1 - f_0(\vec{\mathrm{k}}_1 + \vec{\mathrm{q}})\right]\left[1 - f_0(\vec{\mathrm{k}}_2 - \vec{\mathrm{q}})\right] \\ \times \delta\left(\mathcal{E}(\vec{\mathrm{k}}_1) + \mathcal{E}(\vec{\mathrm{k}}_2) - \mathcal{E}(\vec{\mathrm{k}}_1 + \vec{\mathrm{q}})\right. \\ \left. - \mathcal{E}(\vec{\mathrm{k}}_2 - \vec{\mathrm{q}})\right)\Big\{\psi_1(\vec{\mathrm{k}}_1)\cos\left(\vartheta_{\vec{\mathrm{k}}_1}\right) \\ + \psi_1(\vec{\mathrm{k}}_2)\cos\left(\vartheta_{\vec{\mathrm{k}}_2}\right) - \psi_1\left(\left|\vec{\mathrm{k}}_1 + \vec{\mathrm{q}}\right|\right) \\ \times\cos\left(\vartheta_{\vec{\mathrm{k}}_1+\vec{\mathrm{q}}}\right) - \psi_1\left(\left|\vec{\mathrm{k}}_2 - \vec{\mathrm{q}}\right|\right)\cos\left(\vartheta_{\vec{\mathrm{k}}_2-\vec{\mathrm{q}}}\right)\Big\}\end{aligned} \tag{6}$$

where the integrals are either in 2D ($n = 2$) or 3D ($n = 3$), depending on the system dimensionality. The scattering probability for spin-conserving interactions, w_1, and non-spin-conserving, w_2, interactions is given by:

$$\begin{aligned}w_1\left(\vec{\mathrm{k}}_1 + \vec{\mathrm{q}}\uparrow, \vec{\mathrm{k}}_2 - \vec{\mathrm{q}}\uparrow; \vec{\mathrm{k}}_1\uparrow, \vec{\mathrm{k}}_2\uparrow\right) = \frac{1}{2}\frac{2\pi}{\hbar}\Big|V\left(\vec{\mathrm{q}}, \mathcal{E}(\vec{\mathrm{k}}_1 + \vec{\mathrm{q}}) - \mathcal{E}(\vec{\mathrm{k}}_1)\right) \\ - V\left(\vec{\mathrm{k}}_2 - \vec{\mathrm{q}} + \vec{\mathrm{k}}_1, \mathcal{E}(\vec{\mathrm{k}}_2 - \vec{\mathrm{q}}) - \mathcal{E}(\vec{\mathrm{k}}_1)\right)\Big|^2 \\ \times w_2\left(\vec{\mathrm{k}}_1 + \vec{\mathrm{q}}\uparrow, \vec{\mathrm{k}}_2 - \vec{\mathrm{q}}\downarrow; \vec{\mathrm{k}}_1\uparrow, \vec{\mathrm{k}}_2\downarrow\right) \\ = \frac{1}{2}\frac{2\pi}{\hbar}\left|V\left(\vec{\mathrm{q}}, \mathcal{E}(\vec{\mathrm{k}}_1 + \vec{\mathrm{q}}) - \mathcal{E}(\vec{\mathrm{k}}_1)\right)\right|^2\end{aligned} \tag{7}$$

where $\vec{\mathrm{q}}$ is the phonon momentum. The screened Coulomb potential, $V(\vec{\mathrm{q}}, \mathcal{E})$, is given by:

$$V(\vec{\mathrm{q}}, \mathcal{E}) = \frac{1}{\epsilon(\vec{\mathrm{q}}, \mathcal{E})}\frac{2\pi e^2}{L^2}\frac{1}{q} \tag{8}$$

with the relative dielectric function in the RPA approximation given by (9) [47].

$$\epsilon(\vec{\mathrm{q}}, \mathcal{E}) = 1 - U(\vec{\mathrm{q}})\sum_{\vec{\mathrm{k}}_1}\frac{f_0(\vec{\mathrm{k}}_1 - \vec{\mathrm{q}}) - f_0(\vec{\mathrm{k}}_1)}{\mathcal{E} + \mathcal{E}(\vec{\mathrm{k}}_1 - \vec{\mathrm{q}}) - \mathcal{E}(\vec{\mathrm{k}}_1) + i\hbar\delta} \tag{9}$$

The *spin-averaged* scattering probability ($\bar{w}$) is:

$$\begin{aligned}\bar{w}\left(\vec{\mathrm{k}}_1 + \vec{\mathrm{q}}, \vec{\mathrm{k}}_2 - \vec{\mathrm{q}}; \vec{\mathrm{k}}_1, \vec{\mathrm{k}}_2\right) = \frac{2\pi}{\hbar}\Big\{\Big|V(\vec{\mathrm{q}}, \mathcal{E}(\vec{\mathrm{k}}_1 + \vec{\mathrm{q}}))\Big|^2 \\ - \frac{1}{2}\mathcal{R}e\Big[V\left(\vec{\mathrm{q}}, \mathcal{E}(\vec{\mathrm{k}}_1 + \vec{\mathrm{q}}) - \mathcal{E}(\vec{\mathrm{k}}_1)\right) \\ \times V^*\left(\vec{\mathrm{k}}_2 - \vec{\mathrm{q}} - \vec{\mathrm{k}}_1, \mathcal{E}(\vec{\mathrm{k}}_2 - \vec{\mathrm{q}}) - \mathcal{E}(\vec{\mathrm{k}}_1)\right)\Big]\Big\}\end{aligned} \tag{10}$$

The scattering time, τ_{ee}, can be obtained from (6) assuming:

$$\hat{I}_{ee}\left[\psi_1\cos\left(\vartheta_{\vec{\mathrm{k}}_1}\right)\right] = \frac{\psi_1\cos\left(\vartheta_{\vec{\mathrm{k}}_1}\right)}{\tau_{ee}}. \tag{11}$$

With this result and the wave functions determined in our density functional theory (DFT) calculations, we can determine the scattering time, τ_{ee}, in both the $n = 2$ (2D) and $n = 3$ (3D) limits using:

$$\begin{aligned}\frac{1}{\tau_{ee}(\vec{\mathrm{k}}_1)} \approx 2f_0(\vec{\mathrm{k}}_1)\int \frac{d^n q}{(2\pi)^n}\left[1 - f_0(\vec{\mathrm{k}}_1 + \vec{\mathrm{q}})\right] \\ \times \int \frac{d^n k_2}{(2\pi)^n} f_0(\vec{\mathrm{k}}_2)\left[1 - f_0(\vec{\mathrm{k}}_2 - \vec{\mathrm{q}})\right] \\ \times \bar{w}\left(\vec{\mathrm{k}}_1 + \vec{\mathrm{q}}, \vec{\mathrm{k}}_2; \vec{\mathrm{k}}_1, \vec{\mathrm{k}}_2 + \vec{\mathrm{q}}\right) f_0(\vec{\mathrm{k}}_1) \\ \times \delta\left(\mathcal{E}(\vec{\mathrm{k}}_2 + \vec{\mathrm{q}}) - \mathcal{E}(\vec{\mathrm{k}}_2) - \mathcal{E}(\vec{\mathrm{k}}_1 + \vec{\mathrm{q}}) + \mathcal{E}(\vec{\mathrm{k}}_1)\right)\end{aligned} \tag{12}$$

Since the integrals in (12) are performed over momenta $\vec{\mathrm{k}}_2$ and $\vec{\mathrm{q}}$, they are defined by the corresponding density of states (DOS). These results are therefore sensitive to van Hove singularities, Landau levels, and any other sharp peaks in the DOS. The scattering times in the 2D and 3D cases can be different, particularly at low temperature when the thermal broadening of the peaks is suppressed. Figure 5(a) shows the calculated density of states, $\rho(\mathcal{E})$, in 2D and 3D at $B_z = 0$ T taken from Quantum Espresso code, which shows the expected enhancement of the $\rho(\mathcal{E})$ at $\mathcal{E}_\mathrm{F}$ in the 2D limit. We use this density of states to determine the scattering rate, Γ_s, and scattering angle, ϑ, in both limits. The more discrete-like DOS leads to an enhancement in the integral in (12) and, thus, an enhanced scattering rate in the 2D for this contribution to the overall scattering rate. We note again that this is only the leading contribution to (2), while the other contributions to this include additional scattering mechanisms (e.g. electron–phonon, electron–impurity, etc), which would not conserve momentum and transfer some to the lattice degrees of freedom.

3.2. Scattering distribution, $S(\vartheta)$, in 2D and 3D

To gain insight on the different contributions, we determine an approximate theoretical form for the distribution of scattering

angles, $S(\vartheta)$. An electron with a momentum $\vec{\mathrm{k}}_1$ scatters to the new momentum $\vec{\mathrm{k}}_1{}' = \vec{\mathrm{k}}_1 + \vec{\mathrm{q}}$, while a second electron scatters from $\vec{\mathrm{k}}_2 = \vec{\mathrm{k}}_2{}' - \vec{\mathrm{q}}$ to a new momentum $\vec{\mathrm{k}}_2$. The angle-dependence of the scattering will determined by the integrand of (12):

$$S(\vartheta) = \left[1 - f_0\left(\vec{\mathrm{k}}_1 + \vec{\mathrm{q}}\right)\right] \int \mathrm{d}\gamma \Bigg\{ f_0\left(\vec{\mathrm{k}}_2\right)\left[1 - f_0\left(\vec{\mathrm{k}}_2 - \vec{\mathrm{q}}\right)\right] \times \bar{w}\left(\vec{\mathrm{k}}_1 + \vec{\mathrm{q}}, \vec{\mathrm{k}}_2; \vec{\mathrm{k}}_1, \vec{\mathrm{k}}_2 + \vec{\mathrm{q}}\right) \delta\Big(\mathcal{E}\left(\vec{\mathrm{k}}_2 + \vec{\mathrm{q}}\right) - \mathcal{E}\left(\vec{\mathrm{k}}_2\right) - \left[\mathcal{E}\left(\vec{\mathrm{k}}_1 + \vec{\mathrm{q}}\right) - \mathcal{E}\left(\vec{\mathrm{k}}_1\right)\right]\Big) \Bigg\} \tag{13}$$

Assuming that the change to the momenta is small, we can approximate $\left|\vec{\mathrm{k}}_1\right| \approx \left|\vec{\mathrm{k}}_2\right| \approx \left|\vec{\mathrm{k}}_1{}'\right|$, which are all approximately equal to the magnitude of the Fermi vector, $\left|\vec{k}_\mathrm{F}\right|$. Within the effective mass approximation, the distribution, $S_{2D}(\vartheta)$, of scattering angles in the 2D case is:

$$S_{2D}(\vartheta) \approx \frac{\pi}{2\hbar}\left(\frac{2\pi e^2}{\epsilon_0 L}\right)^2 \left(\frac{\kappa}{k_\mathrm{F}^3}\right) \left[\frac{1}{\left(\vartheta + \frac{\kappa}{k_\mathrm{F}}\right)^2 \left(\vartheta + 2\frac{\kappa}{k_\mathrm{F}}\right)}\right] \times \frac{1}{\left\{\exp\left(\frac{\hbar^2 k_\mathrm{F}^2}{2m^* k_\mathrm{B} T}\vartheta^2\right) + 1\right\}} \tag{14}$$

where k_F is the magnitude of the Fermi vector, T is the temperature, L is the quantum well width, and $\kappa = \frac{2\pi e^2}{\epsilon_0}\frac{\partial n}{\partial \mu}$ is the inverse screening length in 2D. In contrast, we see that $S_{3D}(\vartheta)$ in a 3D system is:

$$S_{3D}(\vartheta) \approx \frac{\pi}{2\hbar}\left(\frac{4\pi e^2}{\epsilon_0 L^3}\right)^2 \left(\frac{1}{k_\mathrm{F}^4}\right) \left[\frac{1}{\left(\vartheta + \frac{\kappa^2}{k_\mathrm{F}^2}\right)^2}\left(\frac{6\frac{\kappa^2}{k_\mathrm{F}^2}}{\vartheta^2 + 4\frac{\kappa^2}{k_\mathrm{F}^2}} - 1\right)\right] \times \frac{1}{\left\{\exp\left(\frac{\hbar^2 k_\mathrm{F}^2}{2m^* k_\mathrm{B} T}\vartheta^2\right) + 1\right\}} \tag{15}$$

where $\kappa = \sqrt{\frac{4\pi e^2}{\epsilon_0}\frac{\partial n}{\partial \mu}}$ is the inverse screening length in 3D (the appropriate unit for the factor $\frac{4\pi e^2}{\epsilon_0}$ is [energy times distance], thus both 2D and 3D inverse screening lengths have units of [1/distance]). From these *in both 2D and 3D*, we can see that scattering is suppressed when $\left\{\exp\left(\frac{\hbar^2 k_\mathrm{F}^2}{2m^* k_\mathrm{B} T}\vartheta^2\right) + 1\right\} \gg 1$, which occurs when $\frac{\hbar^2 k_\mathrm{F}^2}{2m^* k_\mathrm{B} T}\vartheta^2 \gg 1$. The narrowing of the distribution leads to an enhancement in the dephasing time at low temperatures in both the 2D and the 3D samples, which is only observable in EA0745 in our data given its much longer τ_m [48].

4. Numerical calculations

We demonstrate the important role that the distribution of scattering angles, $S(\vartheta)$, has on the dephasing time in figure 6. The samples that we study have important contributions to (2)

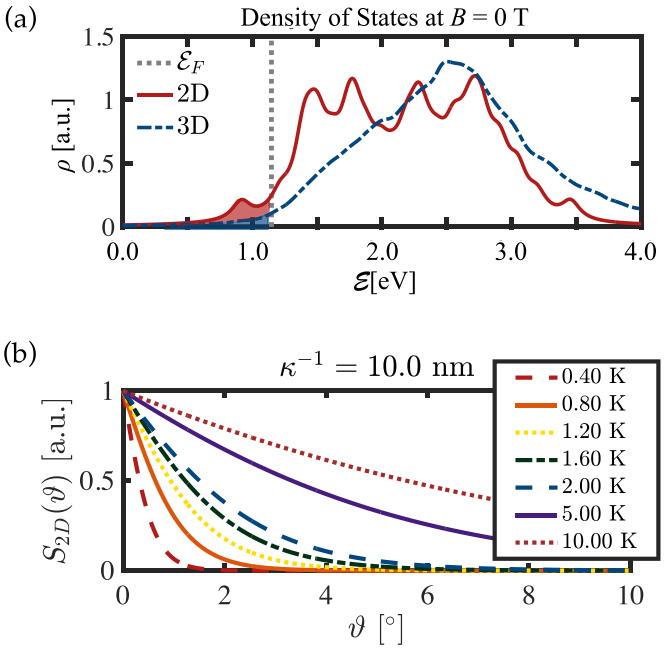

Figure 5. (a) This is the calculated density of states, $\rho(\mathcal{E})$, in both the 2D and 3D limits in GaAs at $\mathbf{B} = 0$ T, showing the enhancement of the $\rho(\mathcal{E})$ in 2D when compared to 3D. (b) S_{2D} with a screening length of $\kappa^{-1} = 10$ nm, showing the narrowing of the scattering distribution as temperature is lowered.

from carrier-carrier, carrier-phonon, and carrier-impurity scattering [49] and our DFT-based modeling has demonstrated the leading term in the electron–scattering time in (12). Electron–electron scattering conserves momentum [50], so in this section we demonstrate through a numerical simulation how this can nonetheless dominate the dephasing time, τ_2, absent process that would transfer momentum to the lattice or impurities.

Figure 6(a) shows a schematic of a momentum-conserving scattering process in a cyclotron [48]. An analogy here is the phenomena of momentum relaxation in no external magnetic field after femtosecond subband-to-subband excitation [51], which rapidly relaxes the initial momentum distribution in each of the subbands towards a Boltzmann distribution with a lifetime on the order of $\tau_m \sim 150$ fs [52]. In cyclotron decay, the electron begins the classical circular orbit at point A and scatters through an angle, ϑ, at point B in the diagram (from $\hbar\vec{k}_i$ to $\hbar\vec{k}_f$). The change in momentum, $\hbar\vec{\mathrm{k}}_{1\,\delta}$, is transferred to a second cyclotron (from $\hbar\vec{k}_i'$ to $\hbar\vec{k}_f'$), preserving the total momentum of the interacting cyclotrons and transferring $\hbar\vec{k}_\delta$ between the interacting cyclotrons. These scattering interactions occur in the ensemble of electrons, with a probability distribution of angles governed by $S(\vartheta)$ in equations (14) and (15), depending on the dimensionality of 2DEG.

We model the scattering of an ensemble of cyclotrons assuming a constant uniform scattering rate, Γ_q, and vary the width of the scattering distribution (see figure 5(b)) to isolate the component of τ_2 resulting from the distribution of scattering angles, $S(\vartheta)$. This is a simplification, of course, as both the scattering distribution width and rate would vary with

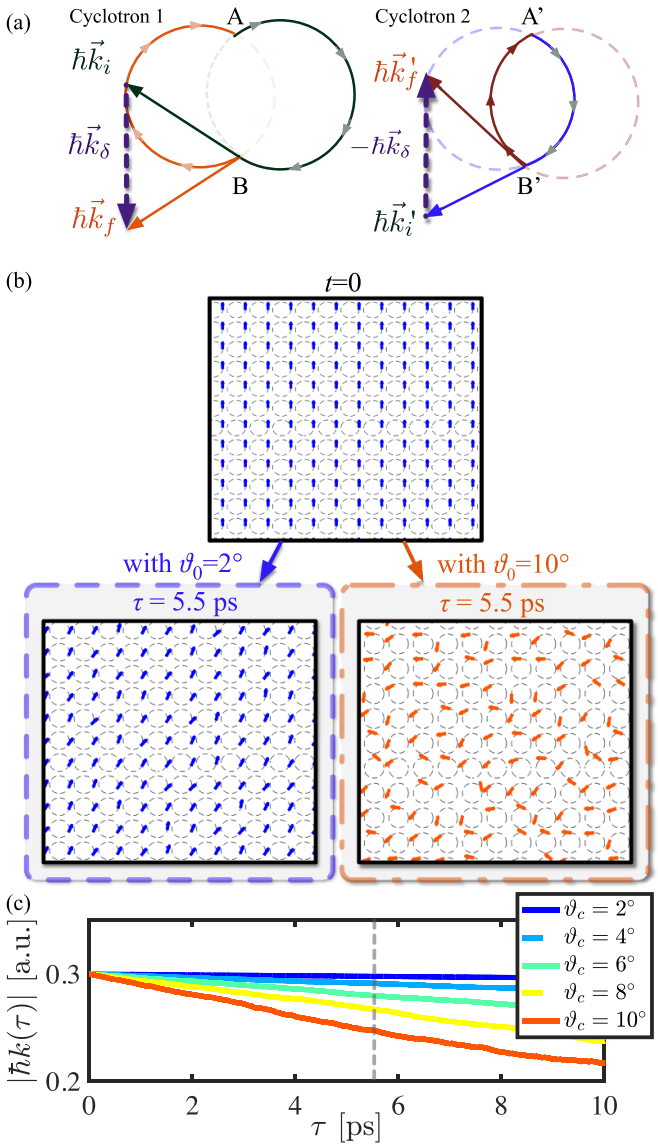

Figure 6. (a) A schematic of momentum transfer, $\hbar\vec{k}_\delta$, from one cyclotron (on the right) to a second cyclotron (on the left). (b) The results of the numerical model demonstrating the role of the scattering angle, $S(\vartheta)$, in dephasing. The top panel shows the initial distribution, $\hbar\vec{k}$, of cyclotrons at $t = 0$ in the center of mass reference frame. For a constant scattering rate of $\Gamma = (1.1\,\mathrm{ps})^{-1}$, the second level of figures shows the ensemble at $t = 5.5\,\mathrm{ps}$ for two different scattering angle limits, θ_0, as described in the text. The bottom panel plots the magnitude of the Bloch vector, $|\hbar\vec{k}|$, for the ensemble as a function of time for a range of θ_0.

temperature. Figure 6(b) shows a subset of these N cyclotrons, which begin in phase at $t = 0$ and scatter with a constant rate of $\Gamma_q = (1.1\,\mathrm{ps})^{-1}$ with a cutoff scattering angle, ϑ_0 of 2° (left) or 10° (right). The difference in the ensemble order is clear at $\tau = 5.5\,\mathrm{ps}$, with little variation in the direction of $\hbar\vec{k}$ when $\vartheta_0 = 2°$ but a significantly larger loss of order when $\vartheta_0 = 10°$. Dephasing results in a reduction in the ensemble Bloch vector, as shown figure 6(c), for a range of cutoff scattering angles [53], which shows a five-fold increase in the simulated dephasing time when the cut off angle is reduced from 10° to 2°. Thus, both the scattering rate from the DFT calculations as

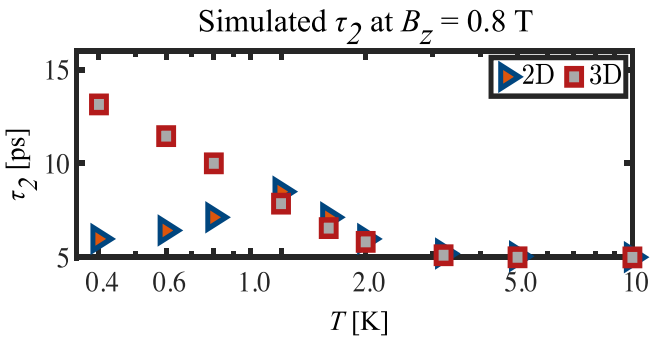

Figure 7. DFT predicted scattering time in the 2D and 3D limits. The difference in τ_2 in the two samples below $T \leqslant T_0$ results from the much faster scattering rate, Γ_s, and narrower angular distribution in the 2D limit.

well as the temperature-dependent scattering distribution contribute to τ_2.

5. Final results

Figure 7 shows the final model of the electron–scattering contribution to the dephasing rate, combining the scattering simulation from the DFT modeling with $S(\vartheta)$. The quantitative agreement between our calculation and the simulation is, of course, not exact and predicts a faster τ_2 than we observe in figure 4(c). Significant, however, is the prediction of a crossover temperature above which both samples would be limited by the scattering time/angle. This shorter dephasing time that we find in our simulation, in part, may be a limitation of the Quantum Espresso/DFT codes that we use, which underestimates the band structure parameters in GaAs. Also, as shown in figure 4(b) the determination of the dephasing time is sensitive to the uncertainty in n_s. It is likely that a modified DFT code that could more accurately reproduce our electronic band structure would also better predict the scattering rate and angle.

6. Conclusions

We have studied cyclotron dephasing and superradiant emission as a function of temperature at $B_z = 0.8\,\mathrm{T}$ in both a narrow and wide quantum well to elucidate the effects of quantum confinement in 2DEG's. Both sets of experimental data show good agreement in dephasing rates above $T_0 = 1.2\,\mathrm{K}$, but show significant deviations below. The dephasing time, τ_2, decreases in the narrow QW (VA0607) primarily due to the enhancement of the density of states at the Fermi edge as well as the importance of interface scattering in this sample. In the wide quantum well (EA0745), the substantial reduction in the scattering angle distribution at low temperatures enhances the dephasing time beyond what can be explained by the reduced scattering rate within the quasi-3D limit. This result will be a significant detrimental component of future quantum device designs [54], where reduced dimensionality will be accompanied by an decrease in dephasing time. Mitigation of

this effect may be possible in monolayer materials like the transition metal dichalcogenides, where the strong enhancement due to quantum confinement may be partly offset by the reduced screening [4].

Data availability statement

The data cannot be made publicly available upon publication because they are not available in a format that is sufficiently accessible or reusable by other researchers. The data that support the findings of this study are available upon reasonable request from the authors.

Acknowledgments

Experiments (BB, AL, AO, JC, and DH) were supported by the Department of Energy (DE-SC0019137). Theory calculations (VT) were supported by the US Department of Energy (DE-FG02-07ER46354). A portion of this work was performed at the National High Magnetic Field Laboratory, which is supported by National Science Foundation Cooperative Agreement No. DMR-1644779 and the State of Florida. This work was performed, in part, at the Center for Integrated Nanotechnologies, an Office of Science User Facility operated for the U.S. Department of Energy (DOE) Office of Science. Sandia National Laboratories is a multimission laboratory managed and operated by National Technology & Engineering Solutions of Sandia, LLC, a wholly owned subsidiary of Honeywell International, Inc. for the U.S. DOE's National Nuclear Security Administration under contract DE-NA-0003525. The views expressed in the article do not necessarily represent the views of the U.S. DOE or the United States Government. The data that support the findings of this study are available upon request from the authors.

ORCID iDs

B Barman https://orcid.org/0000-0003-4228-6046
S A McGill https://orcid.org/0000-0001-6365-7155
V Turkowski https://orcid.org/0000-0003-0762-0002
D J Hilton https://orcid.org/0000-0003-2058-9062

References

[1] Averitt R D and Taylor A J 2002 *J. Phys.: Condens. Matter* **14** R1357–90
[2] Karaiskaj D, Bristow A D, Yang L, Dai X, Mirin R P, Mukamel S and Cundiff S T 2010 *Phys. Rev. Lett.* **104** 117401
[3] Turner D B and Nelson K A 2010 *Nature* **466** 1089–91
[4] Moody G *et al* 2015 *Nat. Commun.* **6** 136805
[5] Almand-Hunter A E, Li H, Cundiff S T, Mootz M, Kira M and Koch S W 2014 *Nature* **506** 471–5
[6] Dey P, Paul J, Wang Z, Stevens C E, Liu C, Romero A H, Shan J, Hilton D J and Karaiskaj D 2016 *Phys. Rev. Lett.* **116** 127402
[7] Haider G *et al* 2021 *Adv. Funct. Mater.* **31** 2102196
[8] Mak K F, He K, Lee C, Lee G H, Hone J and Heinz T F 2013 *Nat. Mater.* **12** 207–11
[9] Wang Q *et al* 2020 *Nano Lett.* **20** 7193–9
[10] Vogt P, De Padova P, Quaresima C, Avila J, Frantzeskakis E, Asensio M, Resta A, Ealet B and Le Lay G 2012 *Phys. Rev. Lett.* **108** 155501
[11] Dávila M E and Le Lay G 2016 *Sci. Rep.* **6** 20714
[12] Zhu F-F, Chen W-J, Xu Y, Gao C-L, Guan D-D, Liu C-H, Qian D, Zhang S-C and Jia J-F 2015 *Nat. Mater.* **14** 1020–5
[13] Liu H, Neal A T, Zhu Z, Luo Z, Xu X, Tománek D and Ye P D 2014 *ACS Nano* **8** 4033–41
[14] Zhang J L *et al* 2016 *Nano Lett.* **16** 4903–8
[15] Dicke R H 1954 *Phys. Rev.* **93** 99–110
[16] Jho Y D, Wang X, Kono J, Reitze D H, Wei X, Belyanin A A, Kocharovsky V V, Kocharovsky V V and Solomon G S 2006 *Phys. Rev. Lett.* **96** 237401
[17] Wang H Z, Zheng X G, Zhao F L, Gao Z L and Yu Z X 1995 *Phys. Rev. Lett.* **74** 4079–82
[18] Gaal P, Reimann K, Woerner M, Elsaesser T, Hey R and Ploog K H 2006 *Phys. Rev. Lett.* **96** 187402
[19] Skribanowitz N, Herman I P, MacGillivray J C and Feld M S 1973 *Phys. Rev. Lett.* **30** 309–12
[20] Rajabi F and Houde M 2016 *Astrophys. J.* **826** 216
[21] Houde M, Mathews A and Rajabi F 2018 *Mon. Not. R. Astron. Soc.* **475** 514–22
[22] Abdussalam W and Machnikowski P 2014 *Phys. Rev.* B **90** 125307
[23] Zhang Q *et al* 2014 *Phys. Rev. Lett.* **113** 047601
[24] Curtis J A, Tokumoto T, Hatke A T, Cherian J G, Reno J L, McGill S A, Karaiskaj D and Hilton D J 2016 *Phys. Rev.* B **93** 155437
[25] Wang X, Hilton D J, Reno J L, Mittleman D M and Kono J 2010 *Opt. Exp.* **18** 12354–61
[26] Wang X, Hilton D J, Ren L, Mittleman D M, Kono J and Reno J L 2007 *Opt. Lett.* **32** 1845–7
[27] Schmuttenmaer C A 2004 *ACS Publ.* **104** 1759–80
[28] Auston D H, Cheung K P and Smith P R 1984 *Appl. Phys. Lett.* **45** 284–7
[29] van Exter M, Fattinger C and Grischkowsky D 1989 *Opt. Lett.* **14** 1128
[30] Störmer H L, Dingle R, Gossard A C, Wiegmann W and Sturge M D 1979 *Solid State Commun.* **29** 705–9
[31] Dingle R, Störmer H L, Gossard A C and Wiegmann W 1978 *Appl. Phys. Lett.* **33** 665
[32] Some D and Nurmikko A V 1994 *Appl. Phys. Lett.* **65** 3377–9
[33] Maan J C, Englert T, Tsui D C and Gossard A C 1982 *Appl. Phys. Lett.* **40** 609
[34] Sigg H, Wyder P and Perenboom J A 1985 *Phys. Rev.* B **31** 5253–61
[35] Seidenbusch W, Gornik E and Weinmann G 1987 *Phys. Rev.* B **36** 9155–9
[36] Liu C T, Mensz P, Tsui D C and Weimann G 1989 *Phys. Rev.* B **40** 1716–9
[37] Cheng J-P and McCombe B D 1990 *Phys. Rev. Lett.* **64** 3171–4
[38] Huggard P G, Cluff J A, Shaw C J, Andrews S R, Linfield E H and Ritchie D A 1997 *Appl. Phys. Lett.* **71** 2647
[39] Chou M, Tsui D and Weimann G 1988 *Phys. Rev.* B **37** 848–54
[40] Schlesinger Z, Wang W and MacDonald A H 1987 *Phys. Rev. Lett.* **58** 73–76
[41] Kriisa A, Samaraweera R L, Heimbeck M S, Everitt H O, Reichl C, Wegscheider W and Mani R G 2019 *Sci. Rep.* **9** 1–10
[42] Chauhan P, Thomas C, Lindemann T, Gardner G C, Gukelberger J, Manfra M J and Armitage N P 2022 *Appl. Phys. Lett.* **120** 142105
[43] Chung Y J, Villegas Rosales K A, Baldwin K W, Madathil P T, West K W, Shayegan M and Pfeiffer L N 2021 *Nat. Mater.* **20** 632–7
[44] Das Sarma S, Hwang E H, Kodiyalam S, Pfeiffer L N and West K W 2015 *Phys. Rev.* B **91** 205304

[45] Hilton D J 2012 *Opt. Exp.* **20** 29717–26
[46] Isar A, Sandulescu A, Scutaru H, Stefanescu E and Scheid W 1994 *Int. J. Mod. Phys.* E **03** 635–714
[47] Hu B Y K and Flensberg K 1996 *Phys. Rev.* B **53** 10072–7
[48] Terwilliger D W and Higgins R J 1973 *Phys. Rev.* B **7** 667–73
[49] Lee K, Shur M S, Drummond T J and Morkoç H 1983 *J. Appl. Phys.* **54** 6432
[50] Ridley B K 2000 *Quantum Processes in Semiconductors* 4th edn (Oxford: Oxford University Press)
[51] Ganikhanov F, Burr K C, Hilton D J and Tang C L 1999 *Phys. Rev.* B **60** 8890–6
[52] Tommasi R, Langot P and Vallée F 1996 *Appl. Phys. Lett.* **66** 1361–3
[53] Kropf C M 2020 *Phys. Rev. Res.* **2** 033311
[54] Scalari G *et al* 2012 *Science* **335** 1323–6